Catalytic methanation of CO and CO2 in coke oven gas over Ni–Co/ZrO2–CeO2

6 AUTHORS, INCLUDING:

Rauf Razzaq
University of Engineering and Technology, La…
14 PUBLICATIONS   146 CITATIONS

SEE PROFILE

Dr. Muhammad Usman
Tsinghua University
10 PUBLICATIONS   72 CITATIONS

SEE PROFILE

Chunshan Li
Chinese Academy of Science, China, Bejing
80 PUBLICATIONS   957 CITATIONS

SEE PROFILE

Catalytic Methanation of CO and CO_2 in Coke Oven Gas over Ni–Co/ ZrO_2–CeO_2

Rauf Razzaq, Hongwei Zhu, Li Jiang, Usman Muhammad, Chunshan Li,* and Suojiang Zhang*

Beijing Key Laboratory of Ionic Liquids Clean Process, State Key Laboratory of Multiphase Complex Systems, Institute of Process Engineering, Chinese Academy of Sciences, Beijing 100190, PR China

ABSTRACT: The methanation of CO and CO_2 present in coke oven gas was performed in a fixed-bed catalytic reactor at a reaction temperature between 200 and 400 °C. Different support materials, including SiO_2, Al_2O_3, ZrO_2, and CeO_2, were doped with a different percentage of active metals using a standard impregnation and coprecipitation method. The catalysts were characterized using Brunauer–Emmett–Teller analysis, scanning electron microscopy, X-ray diffraction, X-ray photoelectron spectroscopy, and temperature-programmed desorption techniques. The activity of all samples was tested in terms of the percentage of CO and CO_2 conversion and CH_4 selectivity. The results were analyzed on the basis of the difference in the catalytic performance at different active metal loadings and support materials. The effect of the catalytic support on the reducibility, morphology, and active metal dispersion was investigated. The ZrO_2–CeO_2-supported catalyst prepared under coprecipitation can attain 100% CO conversion at around 300 °C and ≥95% CO_2 conversion at 400 °C and has a CH_4 selectivity of 99%.

1. INTRODUCTION

The coke oven gas (COG) is a byproduct from coking plants during the blast furnace coke production at approximately 800 °C. The gas obtained after removal of NH_3, H_2S, and other hydrocarbons consists of 55 to 58 vol% H_2, 25 to 27 vol% CH_4, 6.5 to 7 vol% CO, 3 to 3.5 vol% CO_2, and 3.5 to 4 vol% N_2. The annual COG production in China for 2007 was estimated at 70 billion Nm^3. Although some of this gas is used on-site as fuel in the coke ovens and in other processes in the steel industry, most of it is either directly discharged into the atmosphere or burned in torches, resulting in serious environmental consequences and considerable waste of valuable energy. Developing new technologies to recover and utilize COG from the steel industry is therefore urgently needed.[1−4]

Over the past few years, COG has been highly investigated as an important source of H_2, synthetic gas (syn-gas), and methanol.[3,5−7] The amplification of the CH_4 present in COG through the catalytic hydrogenation of CO and CO_2 is regarded as a simple and highly efficient way of producing a gas with high calorific value and wide industrial and commercial use. The methanation reaction has been extensively used for the removal of carbon oxides from gas mixtures in ammonia plants, from H_2 purification in refineries, and from ethylene plants.[8] Sabatier and Senderens[9] first studied the methanation reaction at the beginning of the 20th century. Ni and other metals (Ru, Rh, Pt, Fe, and Co) were found to catalyze the reaction of CO in the presence of H_2 to produce CH_4 and water.[10] The choice and preparation of a catalyst is the most crucial stage of CH_4 synthesis from COG. The methanation of CO_2 is more rapid and more selective compared with that of CO over Ni, Fe, Rh, and Ru catalysts. However, this phenomenon only occurs in the case of solo CO_2 methanation. During comethanation of CO and CO_2, CO_2 methanation is completely suppressed until a very high conversion of CO is attained.[11] Ni is the most widely applied and studied methanation catalyst because of its high activity, selectivity, and relatively low price. Ni based catalysts are also preferred for exothermic reactions due to their high heat conductivity, providing better control over the heat of the reaction and allowing a higher catalytic conversion to be maintained within the isothermal conditions of the catalyst bed.[12,13] However, Ni-based catalysts are also more vulnerable to coking, which may lead to catalyst deactivation as well as reactor plugging. The problem particularly occurs either through CH_4 decomposition or via a CO disproportionation reaction. Coking can be successfully addressed by adding certain metalloids, such as boron, that act by suppressing the crystalline carbon formation and improving the thermal stability of Ni-based catalysts. The use of Ni–Co as a bimetallic catalyst has also reportedly improved the coking resistance.[14] Different supports have been used to disperse Ni and other active metal particles on the catalyst surface. These supports include Al_2O_3, TiO_2, zeolites, and SiO_2. The activity and selectivity of the supported metal catalysts are strongly affected by the amount of metal loading, the size of the dispersed metal particles, the interactions between the support and the active species, and the composition of the support material.[15] Abe et al.[16] demonstrated the importance of the metal size distribution over the support by loading Ru nanoparticles on a TiO_2 support, resulting in higher product yield and activity for CO_2 methanation. Bimetallic catalysts were given prime importance over the past decade to enhance the catalyst activity. Experimental results have confirmed that bimetallic Ni–Fe alloys are more active than the traditional monometallic Ni and Fe catalysts for CO methanation. Catalyst performance can be increased by varying the Ni:Fe ratio, the total metal loading,

and the support material. A catalytic composition of 75Ni25Fe over a $MgAl_2O_4$ support at 20 wt % total metal loading was found to be the most active and selective for CH_4.[17] Bimetallic $Ni-Mo/Al_2O_3$ catalysts prepared via coimpregnation have also been previously studied for CO_2 methanation; the Ni active sites were strongly affected by the interaction between Ni and Mo.[18] Ocampo et al.[19] established that a Ni-based mixed oxide catalyst with a 60:40 CeO_2/ZrO_2 ratio, prepared via the sol−gel method, exhibited the highest catalytic activity for CO_2 conversion. Moreover, the addition of a noble metal led to higher Ni dispersion, increasing both the activity and lifetime of the catalyst. Sharma et al.[20] investigated the CO_2 methanation catalyzed by CeO_2, which was doped with Ni, Co, Ru, and Pd via a combustion method. The Ru/CeO_2 catalyst exhibited the highest activity, converting 55% of CO_2 with a CH_4 selectivity of 99% at 450 °C. The use of ZrO_2 as a promoter for a Ni/SiO_2 catalyst enhances Ni dispersion over the surface of SiO_2, resulting in high catalytic activity and complete CO conversion to CH_4 at approximately 240 °C.[21] A combination of two promoters, La and Ru, provided the best catalyst performance for the conversion of CO and H_2 to CH_4 for alumina-supported Co catalysts using an incipient wetness impregnation method.[22] The catalytic activity for a feed gas containing a CO/CO_2 mixture is poor because of the promotion of an undesired reverse water−gas shift reaction (RWGSR). However, the addition of 30% water vapor (steam) in the feed inhibits the RWGSR, resulting in enhanced CO hydrogenation. Results showed that CO conversion over Ru-carbon nanofiber catalysts increases two- to three-fold in the presence of steam.[23,24] Preferential CO methanation has also been recently studied over a 10 wt % Ni/CeO_2 catalyst using a fixed bed reactor incorporating an integrated heat exchanger. The nickel-ceria catalyst showed high methanation activity and selectivity in the reformate gas over a wide temperature interval (250−300 °C).[25]

Investigations on the role of a mixed support in the catalytic methanation of CO and CO_2 have rarely been conducted. The current study reports the overall CO_x methanation of COG to produce a clean gas with high calorific value and improved industrial and commercial use. The effect of different active metal loadings and support materials on the activity and selectivity of CO and CO_2 methanation was investigated. Different supports were doped with various Ni and other active metals using the impregnation and coprecipitation method. The obtained catalysts were characterized, and the percentage of CO and CO_2 conversion and selectivity toward CH_4 formation were determined. The Ni−Co catalysts with $Al_2O_3-ZrO_2$ and ZrO_2-CeO_2 supports showed the highest catalytic activity in CO and CO_2 methanation.

2. EXPERIMENTAL SECTION

2.1. Catalyst Synthesis. All the gases and reagent chemicals were obtained commercially and used without further purification. Distilled water was used to prepare all aqueous solutions.

Supported catalysts with different active metal loadings were prepared using the conventional coprecipitation method in accordance with the final catalyst composition requirements. $Ni(NO_3)_2 \cdot 6H_2O$ (Santou Xilong Chemicals Ltd., ≥98.0%), $Co(NO_3)_2 \cdot 6H_2O$ (Santou Xilong Chemicals Ltd., ≥99.0%), $Fe(NO_3)_3 \cdot 9H_2O$ (Santou Xilong Chemicals Ltd., ≥98.5%), and $(NH_4)_6Mo_7O_{24} \cdot 4H_2O$ (Santou Xilong Chemicals Ltd., ≥99.0%) were used as active metal precursors. $Al(NO_3)_3 \cdot 9H_2O$

(Santou Xilong Chemicals Ltd., ≥99.0%), $(NH_4)_2Ce(NO_3)_6$ (Sinopharm Chemical Reagent Co. Ltd., 9.0%), $ZrOCl_2 \cdot 8H_2O$ (Sinopharm Chemical Reagent Co. Ltd., 99.0%), and La-$(NO_3)_3 \cdot 6H_2O$ (Sinopharm Chemical Reagent Co. Ltd., 99.0%) were used as support materials. All components were precipitated from the solution using 100 mL of aqueous 0.2 M KOH (Santou Xilong Chemicals Ltd., ≥85.0%) under constant stirring for 1 h. The pH of the solution was maintained at around 9, and the samples were aged for 2 h. The samples were then centrifuged and washed to remove extra water and other unwanted ions. The precipitate was dried in an oven at 120 °C for 9 h. The resulting solid was calcined at 600 °C for 4 h. For comparison, a SiO_2-supported Ni−Co catalyst was also prepared via impregnation. $SiO_2 \cdot 6H_2O$ (Santou Xilong Chemicals Ltd., ≥98.0%) was first calcined at 600 °C for 4 h to remove the water of hydration. The solid SiO_2 support was then impregnated using 0.4 mol/L aqueous $Ni(NO_3)_2 \cdot 6H_2O$ and $Co(NO_3)_2 \cdot 6H_2O$ solutions to form a thick paste. The samples were then ultrasonicated to achieve an efficient active metal dispersion on the surface of the support. The pH was maintained at around 9, and the samples were dried and calcined using the same procedure as for coprecipitation.

All catalysts were initially activated with the reduced mixed gas (∼40% H_2 diluted by Ar) for 3 h at 350 °C and then tested at the given experimental parameters.

2.2. Catalyst Characterization. The specific surface areas (SSAs) of the catalysts were determined from the adsorption−desorption of N_2 at the liquid N_2 temperature using a Quadrasorb SI-MP equipment.

The catalyst morphology was determined via scanning electron microscopy (SEM) using an XL30 S-FEG SEM unit with a 10 kV accelerating voltage. The samples were deposited on a standard aluminum SEM holder and coated with gold. X-ray powder diffraction (XRD) was performed on a Bruker D8 Focus X-ray diffractometer with a Ni-filtered Cu Kα radiation. X-ray photoelectron spectroscopy (XPS) data were obtained using an ESCALab220i-XL electron spectrometer (VG Scientific) with a 300 W Al Ká radiation. The base pressure was approximately 3×10^{-9} mbar. The binding energies (BEs) were referenced to the C 1s line at 284.8 eV from the adventitious carbon.

Temperature-programmed desorption (TPD) of CO was conducted using a Micromerit AutochemII2920. The catalyst sample was pretreated in He for 1 h at 573 K. After cooling to room temperature in Ar, 10%CO/Ar adsorption was performed at 323 K for 1 h. The catalysts were then purged with 30 mL/min He for 1 h to remove the physisorbed CO. The temperature was increased from 323 to 773 K at a rate of 10 K/min. CO_2-TPD was performed on the same instrument at a conventional temperature. The catalyst sample was pretreated in He for 1 h at 573 K and then cooled to room temperature (still under He). CO_2 adsorption was performed at 323 K for 1 h. The catalysts were then purged with 30 mL/min He for 1 h to remove the physisorbed CO_2. The temperature was ramped from 323 to 773 K at a rate of 10 K/min.

2.3. Experimental Setup and Operating Conditions. The experiments were performed in a tubular fixed-bed reactor with 10 mm inner diameter (i.d.) under a 2 MPa pressure. The reactor was located inside an electrically heated and temperature-controlled furnace. A small amount of silicon fiber (5 to 9 μm) was first placed on the catalyst bed, followed by 5 g of SiO_2 (2 to 0.8 mm). The catalyst sample (2.25 g, 0.6 to 0.4 mm) was then introduced into the reactor tubing. A gas

2248

dx.doi.org/10.1021/ie301399z | *Ind. Eng. Chem. Res.* 2013, 52, 2247−2256
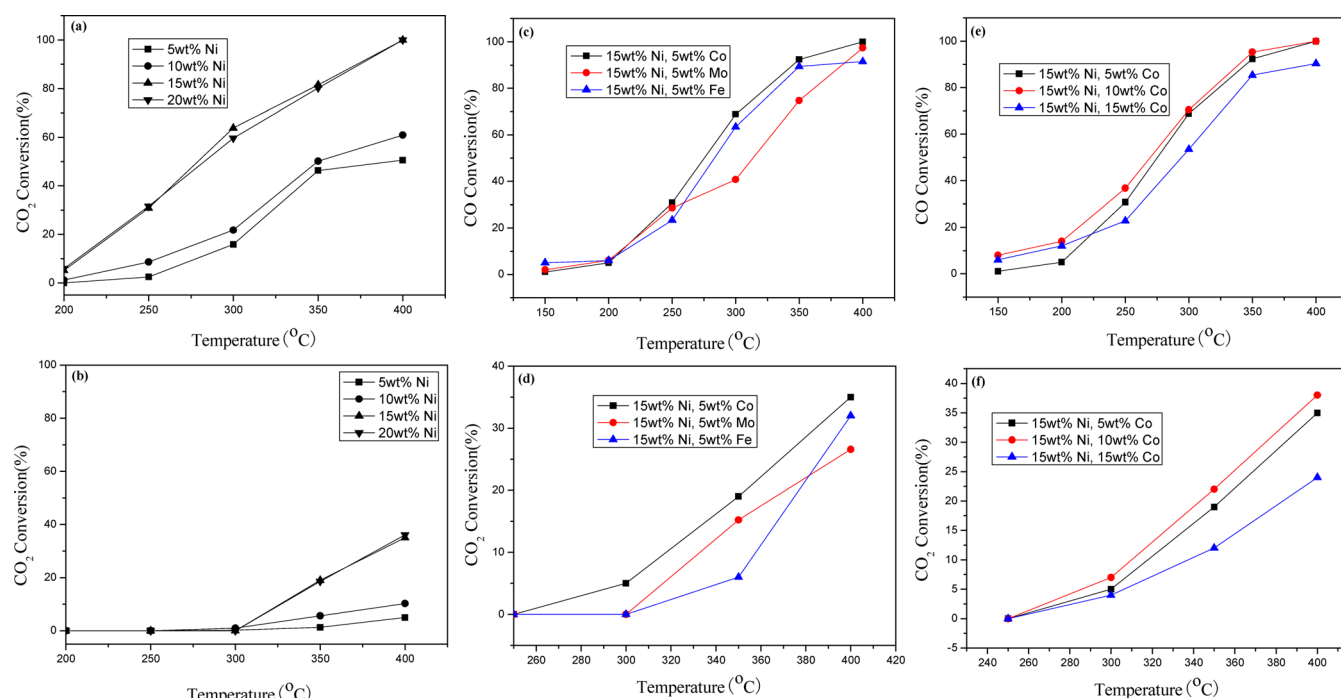
Figure 1. Influence of type and amount of metal loading on overall CO_x methanation activity using Al_2O_3 support: (a) % Ni loading vs CO methanation, (b) % Ni loading vs CO_2 methanation, (c) 5 wt % Fe, Mo, and Co loading vs CO methanation, (d) 5 wt % Fe, Mo, and Co loading vs CO_2 methanation, (e) % Co loading vs CO methanation, and (f) % Co loading vs CO_2 methanation.

mixture containing 7.04% CO, 3.05% CO_2, 4.05% N_2, 27.23% CH_4, and 58.63% H_2 (similar to the composition of COG) was continuously passed through the catalysts with a gas hourly space velocity (GHSV) ranging from 5,000 to 15,000 h^{-1}.

2.4. Calculation and Analysis. After the reaction, the gas mixture was analyzed using an online gas chromatograph equipped with a thermal conductivity detector. The product gases (H_2, N_2, CO, CO_2, and CH_4) were analyzed at temperatures between 200 and 400 °C.

To determine the catalytic activity, the percentage conversion of CO and CO_2 were calculated using eqs 1 and 2. The product selectivity (S_{CH_4}) was determined using eq 3

$$\% \ CO \ conversion: \ X_{CO} = \frac{[M_{CO}]_{In} - [M_{CO}]_{Out}}{[M_{CO}]_{In}} \times 100 \tag{1}$$

$$\% \ CO_2 \ conversion: \ X_{CO_2} = \frac{[M_{CO_2}]_{In} - [M_{CO_2}]_{Out}}{[M_{CO_2}]_{In}} \times 100 \tag{2}$$

$$Product \ Selectivity \ (\%): S_{CH_4}$$
$$= \frac{[M_{CH_4}]_{Out} - [M_{CH_4}]_{In}}{[M_{CO+CO_2}]_{In} - [M_{CO+CO_2}]_{Out}} \times 100 \tag{3}$$

where M is the molar concentration of the inlet and outlet species, and S is the CH_4 selectivity with respect to CO and CO_2.

3. RESULTS AND DISCUSSION

A number of reactions occur during CO and CO_2 methanation, and methane is formed as a result of the competition of such reactions. According to R-1, CO reacts with H_2 to produce CH_4 and H_2O. However, under a low H_2/CO ratio, CO may also be

hydrogenated via reaction R-2 to produce CO_2 which requires a higher H_2/CO_2 ratio to be converted into CH_4 R-3. Undesired water gas shift reaction (WGSR) occurs in accordance with R-4, while another reaction R-5 results in carbon formation having significant impact on activity and lifetime of the catalyst.[10,24]

$$CO + 3H_2 \leftrightarrow CH_4 + H_2O \quad \Delta H^0_{289K} = -206.2 \ kJ/mol \tag{R-1}$$

$$CO + 2H_2 \leftrightarrow CH_4 + CO_2 \quad \Delta H^0_{289K} = -247.3 \ kJ/mol \tag{R-2}$$

$$CO_2 + 4H_2 \leftrightarrow CH_4 + 2H_2O$$
$$\Delta H^0_{289K} = -164.9 \ kJ/mol \tag{R-3}$$

$$CO + H_2O \leftrightarrow CO_2 + H_2 \quad \Delta H^0_{289K} = -41.2 \ kJ/mol \tag{R-4}$$

$$2CO \leftrightarrow C + CO_2 \quad \Delta H^0_{289K} = -172.54 \ kJ/mol \tag{R-5}$$
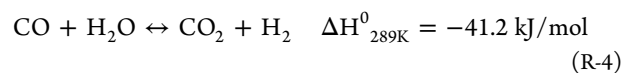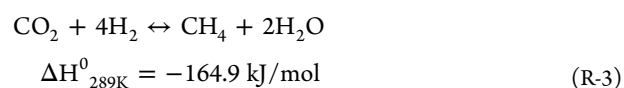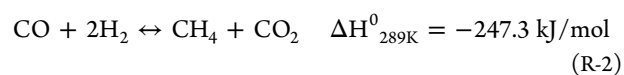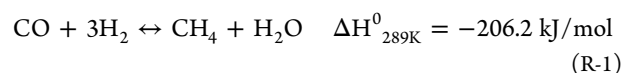
During CO methanation, CO dissociates onto the surface of the catalyst, resulting in the formation of carbon species which are then hydrogenated to produce CH_4.[26] When the methanation of CO starts, CO_2 conversion drops to zero because of the stronger adsorption of CO on the catalyst surface compared with that of CO_2.[27] CO_2 methanation only occurs if the amount of CO in the gas phase is insufficient to trigger CO adsorption. Two main CO_2 methanation routes are proposed in the literature.[28] The first phenomenon involves the dissociative adsorption of CO_2, resulting in the formation of $CO_{(ads)}$ and $O_{(ads)}$, followed by hydrogenation and methanation, which become active in a manner similar to that of CO methanation.[29,30] The second route involves direct CO_2 hydrogenation without the formation of an intermediate CO molecule R-3. Above 300 °C, CO_2 is also produced as a result of WGSR, as water produced in R-1 reacts with CO. Other than

2249

dx.doi.org/10.1021/ie301399z | *Ind. Eng. Chem. Res.* 2013, 52, 2247−2256

WGSR, CO_2 may also be formed via the disproportionation reaction R-5, which, according to the literature,[27] is only applicable in cases of solo-methanation. The reaction temperature must not exceed 400 °C to discourage CO formation via RWGSR, which is favored at elevated temperatures. Panagiotopoulou et al.[31] recognized that at higher temperatures (≥360 °C), the rate of CO production through RWGSR is higher compared with the rate of CO consumption via hydrogenation, resulting in the observed net decrease in X_{CO}. It was also suggested that the rate-determining step in both the CO and CO_2 methanation reactions highly depends on the dissociation of adsorbed CO on the catalyst surface. Therefore, the dissociative adsorption energy of CO is beneficial for a high methanation rate.[8]

3.1. Effect of Active Metal. Al_2O_3-supported catalysts with different metal loadings were first investigated for CO_x methanation activity. The activity was tested under the same experimental conditions as described in section 2.3 with a GHSV of 5,000 h^{-1}. The conversion data are shown in Figure 1(a-f). At all experimental temperatures, an increase in the Ni metal content (up to 15 wt %) led to an increase in the methanation activity. However, as the Ni concentration reached 20 wt % no further improvement was observed. A much higher metal loading may result in blockage of active sites by excess amount of Ni being introduced to the catalyst. Moreover, it may also result in Ni particle agglomeration and poor metal dispersion and can hinder the activity of the catalyst. Fe, Mo, and Co were used as bimetallic catalysts under 5 wt % loading. Results indicate that under the same metal loading Co exhibits the best performance. Further, to investigate the effect of Co loading, Co is also added in different (5, 10, and 15 wt %) metal loading and tested for activity. The activity increased up to 5 wt % Co, while no significant change in activity occurred over 10 wt % loading. However, a significant reduction in activity under 15 wt % Co loading was observed. Under higher metal loading, a reduced activity may be associated with the formation of large metal aggregates resulting in the physical blocking of the external surface of the catalyst. The Ni—Co (3:1) bimetallic catalyst under 20 wt % metal loading showed the best catalytic activity as compared to Ni—Fe and Ni—Mo loaded catalysts.

The Brunauer—Emmett—Teller (BET) SSAs of the catalysts are summarized in Table 1. Results indicate that under the same metal loading (15 wt % Ni and 5 wt % Co) different catalysts exhibit a wide range of SSA (35−390 m^2/g).

Table 1. Type of Catalysts with Their Corresponding Specific Surface Areas

active metal (wt %)	support material	S_{BET} (m^2/g)	preparation method
15%Ni, 5%Co	SiO_2	390	impregnation
15%Ni, 5%Co	Al_2O_3	170	coprecipitation
15%Ni, 5%Co	La_2O_3−Al_2O_3	172	coprecipitation
15%Ni, 5%Co	ZrO_2	35	coprecipitation
15%Ni, 5%Co	Al_2O_3−CeO_2	168	coprecipitation
15%Ni, 5%Co	Al_2O_3−ZrO_2	120	coprecipitation
15%Ni, 5%Co	ZrO_2−CeO_2	105	coprecipitation

XRD results (Figure 2) show low intensity and broad NiO diffraction peaks for the samples incorporating Al_2O_3 support; it is quite reasonable to assume that highly dispersed and much smaller NiO particles may have formed during catalyst preparation. High intensity NiO diffraction peaks at 2θ = 37.2°, 43.3°, and 63.2° appear as shown in Figure 2(b, c),
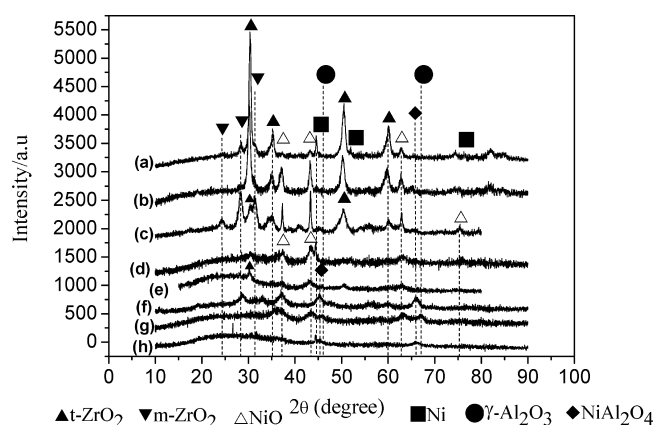
Figure 2. XRD patterns for different supported catalysts with 15 wt % Ni and 5 wt % Co: (a) ZrO_2−CeO_2 (used), (b) ZrO_2−CeO_2 (fresh), (c) ZrO_2 (fresh), (d) Al_2O_3−ZrO_2 (used), (e) Al_2O_3−ZrO_2 (fresh), (f) Al_2O_3−CeO_2 (used), (g) Al_2O_3−CeO_2 (fresh), and (h) La−Al_2O_3 (used).

indicating the formation of larger NiO particles on ZrO_2 and ZrO_2−CeO_2-supported samples. Strong XRD peaks corresponding to metallic Ni are observed at 2θ = 44.508°, 51.847°, and 76.372° for sample (a) indicating that NiO was easily reduced to Ni metal. Other samples including Al_2O_3 support presented more difficulty to be reduced due to the formation of smaller Ni species resulting in strong metal−support interaction. The XRD results for all the samples showed no evidence of a Co crystalline phase, indicating a high degree of Co dispersion over the catalyst surfaces. This high Co dispersion reflects a strong interaction between the metal and the support, which can either reduce the extent of metal reduction or may leave a fraction of some of the Co chemically inactive when reduced, thus influencing the overall activity of the catalyst.[22] Co activity in the catalyst can be influenced by a number of factors, namely, the calcination temperature, type of support material, and the percentage metal loading.

The oxidation states of Ni in the surface region can be determined from the BE and their respective chemical shifts in the XPS spectra.[32] The Ni2p XPS spectra for all the samples (Table 2) shows a ∼1 eV increase in BE after methanation,

Table 2. Binding Energy Values of the Ni−Co/ZrO_2−CeO_2 Catalyst for XPS Spectra

catalyst	binding energy (eV)				
	O1s	Ce3d	Ni2p	Co2p	Zr3d
Ni−Co/Zr-Ce(fresh)	529.3	881.9	854.5	795.4	181.3
Ni−Co/Zr-Ce(reduced)	529.6	882.0	854.8	780.8	181.6
Ni−Co/Zr-Ce(used)	529.7	881.4	855.4	780.0	181.7

indicating the occurrence of atomic sputtering. Ni2p$_{3/2}$ XPS spectrum for the fresh and reduced sample is shown in Figure 3(a, b). The reduced sample exhibited the presence of Ni^0 (B.E 852.7 eV) which was not revealed in the fresh sample. The Ni^0/Ni^{2+} ratio calculated from the designated peak areas increased from 0.34 to 0.4 for the reduced sample indicating a higher concentration of active metal spcies; the results are in agreement with the XRD analysis.

The XPS spectrum for Co2p Figure 3(c) for the fresh sample features a peak at 780.0−781.0 eV which could be mainly attributed to Co_3O_4. The XPS spectra of the used catalyst
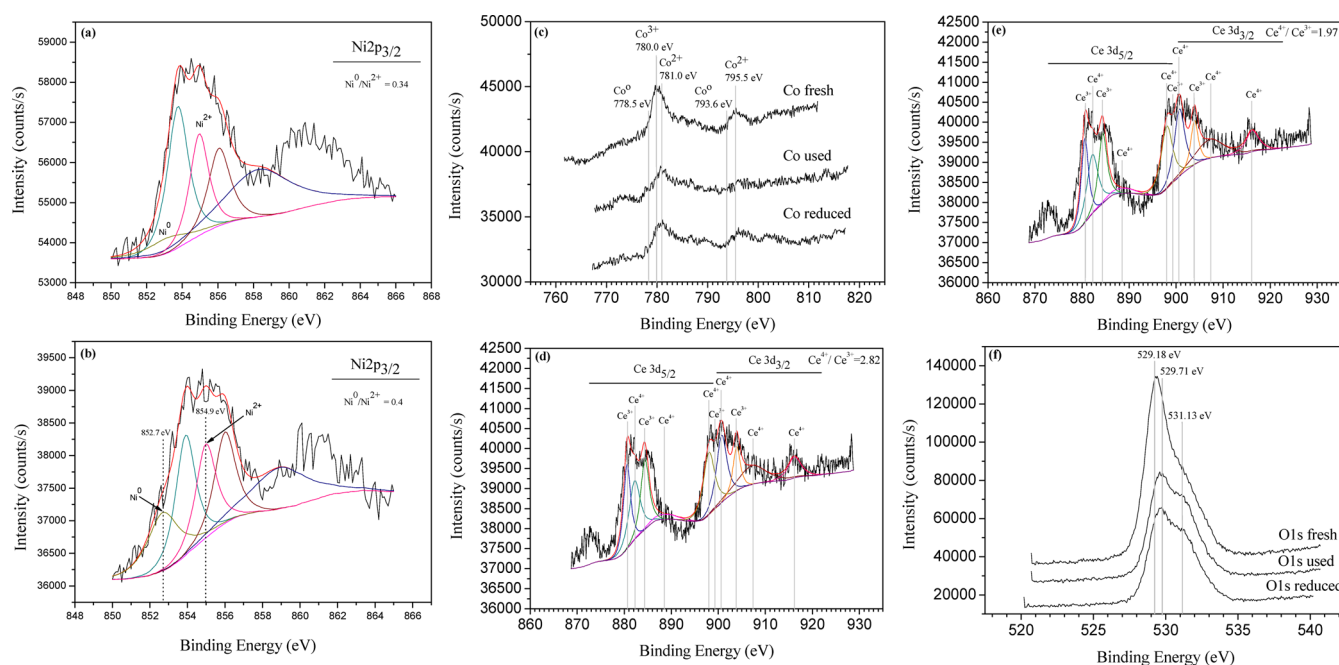
**Figure 3.** XPS spectrum for the Ni−Co/ZrO$_2$−CeO$_2$ catalyst: (a) Ni2p$_{3/2}$ fresh, (b) Ni2p$_{3/2}$ reduced, (c) Co 2p, (d) Ce 3d fresh, (e) Ce 3d used, and (f) O 1s.

shows that the catalyst is partially reduced on the surface as suggested by the intensity increment of the Co(II) shakeup peaks in the Co 2p region (at 787.0 and 804.0 eV).[33]

3.2. Effect of the Support Material. Table 1 shows that the SiO$_2$-supported catalyst prepared via impregnation has the highest SSA, indicating no physical blocking of the support surface with metal containing particles after synthesis and the subsequent thermal treatments. All other catalysts prepared via the coprecipitation method exhibited a reduced SSA as compared to the SiO$_2$-supported impregnated sample. The addition of CeO$_2$ and La$_2$O$_3$ to Al$_2$O$_3$ did not result in any substantial change to SSA, while ZrO$_2$ reduced the SSA of Al$_2$O$_3$ probably due to formation of large oxide aggregates, limiting the access to the internal surface of the catalyst. The ZrO$_2$-supported sample showed the least SSA, indicating metal sintering corresponding to an increased NiO crystallite size as indicated by sharp XRD diffraction peaks. However, CeO$_2$ addition to ZrO$_2$ significantly increased the SSA of the catalyst.

The SEM images of different supported catalysts are shown in Figure 4. All samples show particle agglomeration without any defined geometric shape and size. The addition of CeO$_2$ to Al$_2$O$_3$ had no significant effect on the morphology of the composite oxide support. In addition, the samples incorporating Al$_2$O$_3$ had a spongy appearance. However, the ZrO$_2$−CeO$_2$-supported sample displayed a relatively smother surface with a much darker facade. The SEM image of the ZrO$_2$−CeO$_2$-reduced sample showed a difference in morphology compared with that of its precursor, with smaller grains exhibiting a lower degree of agglomeration.

The XRD patterns for the fresh (calcined) samples are shown in Figure 2 (b, c, e, and g). For the samples with Al$_2$O$_3$ support, no clear and rather weak XRD peaks were observed, which indicates a high degree of multicomponent oxide mixing as well as a high degree of metal dispersion over the support surface. The Al$_2$O$_3$−ZrO$_2$-supported sample (e) exhibited very weak diffraction signals corresponding to a pure tetragonal Zr phase (t-ZrO$_2$) at 2θ = 30.2° and 50.6°. The samples
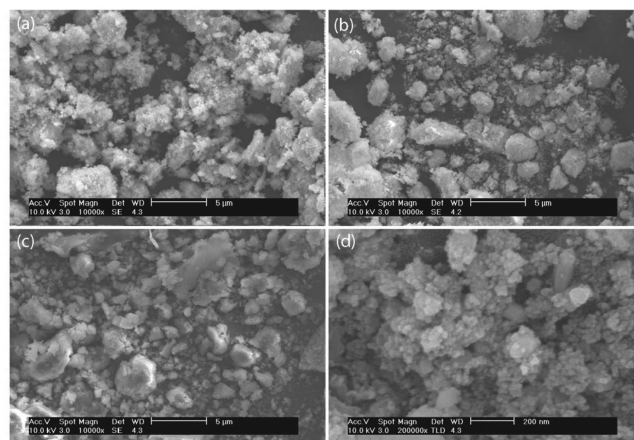
Figure 4. SEM images of different catalysts: (a) Ni−Co/Al, (b) Ni−Co/Al$_2$O$_3$−CeO$_2$, (c) Ni−Co/ZrO$_2$−CeO$_2$ fresh, and (d) Ni−Co/ZrO$_2$−CeO$_2$ reduced.

containing ZrO$_2$ (c) and ZrO$_2$−CeO$_2$ (b) carriers showed narrow and sharp XRD peaks compared with other catalysts, indicating the formation of large crystalline particles. The ZrO$_2$-supported catalyst presented XRD peaks corresponding to a monoclinic Zr phase (m-ZrO$_2$) at 2θ = 24.086°, 28.219°, and 31.503° as well as to a t-ZrO$_2$ phase. The high crystalline pattern of the ZrO$_2$-supported catalyst is in agreement with low SSA mentioned in Table 1. The ZrO$_2$−CeO$_2$-supported sample only showed a segregated and highly crystalline t-ZrO$_2$ phase, indicating that ZrO$_2$ has not been incorporated into the CeO$_2$ lattice. Hernandez et al.[34] established that the addition of 10 wt % CeO$_2$ to ZrO$_2$ helps in stabilizing the tetragonal phase of ZrO$_2$. Both ZrO$_2$−CeO$_2$- and ZrO$_2$-supported samples exhibited sharp XRD peaks corresponding to NiO at 2θ = 37.234°, 43.290°, 62.926°, and 75.357°, indicating that both carriers facilitate the formation of larger NiO crystallites. The XRD patterns of the samples after H$_2$ treatment, as well as their

catalytic activity, are shown in Figure 2 (a, d, f, and h). All reduced samples except Al_2O_3–CeO_2 showed XRD diffractions corresponding to metallic Ni, indicating the successful reduction of NiO. The XRD patterns incorporating Al_2O_3 carrier exhibited cubic γ-Al_2O_3 (JCPDS Card No 10-0425) with diffraction peaks at 2θ = 45.869°, 67.034°. The ZrO_2–CeO_2-supported sample (a) showed strong XRD peaks corresponding to metallic Ni (PDF 00-004-0850) as compared to other catalysts, with peaks at 2θ = 44.508°, 51.847°, and 76.372°. The diffraction peaks indicate that the ZrO_2–CeO_2-supported catalyst presents a more perfect crystal structure, with larger t-ZrO_2 crystallites as well as a metallic Ni phase. The sample also showed a weak XRD diffraction peak at 2θ = 28.5°, which is attributed to m-ZrO_2. This was probably because under subsequent reduction and catalytic activity some of the t-ZrO_2 was converted into m-ZrO_2. The addition of Al_2O_3 to ZrO_2 support promotes metal–support interaction, producing a smaller and well-distributed crystalline size. Srisiriwat et al.[35] concluded that ZrO_2 can be amorphous or can interact with Al_2O_3, thereby inhibiting the interaction between Ni and alumina to form $NiAl_2O_4$ spinel. However, the CeO_2–Al_2O_3-supported sample exhibited characteristic peaks at 2θ = 45.039° and 65.590° attributing to $NiAl_2O_4$ (JCPDS Card No 73-0239). The formation of $NiAl_2O_4$ crystals by the Ce–Al sample may be due to the interaction between Ni and the alumina support in the reaction environment at elevated temperatures. Oh et al.[36] reported that the formation of $NiAl_2O_4$ crystals is favorable at high temperatures in their investigation on Ni/Ce–ZrO_2–Al_2O_3 catalysts. Such formation discourages the appearance of a separate Ni-phase, such as NiO or metallic Ni, and may affect the catalytic activity. The elemental oxidation states of Ce (Figure 3 d, e) on the surface of the Ni–Co/ZrO_2–CeO_2 catalyst were investigated by XPS. The spectrum was fitted using Gaussian distributions, and the peak positions and areas were determined (Table 2). The Ce 3d Gaussian peak fits corresponding to Ce^{4+} and Ce^{3+} states were marked based on some previous studies on CeO_2 XPS analysis.[37−39] The high resolution spectra corresponding to Ce $3d_{3/2}$ and Ce $3d_{5/2}$ ionization features were fitted under ten Gaussian distributions representing the initial and final oxidation states in Ce 3d core level XPS spectra (Figure 3 (a, b)). The difference in Ce $3d_{3/2}$ and Ce $3d_{5/2}$ binding energies varied between 18.15 and 19.5 eV in comparison to a standard expected value of 18.6 eV. In the Ce 3d XPS spectrum, peaks marked at 900.7, 907.2, and 916.15 eV were arising from Ce^{4+} $3d_{3/2}$, while the bands marked at 882.2, 888.6, and 898.0 eV arise from Ce^{4+} $3d_{5/2}$. Similarly the bands at 899.3 and 903.9 eV were due to Ce^{3+} $3d_{3/2}$, and those at 880.6 and 884.6 eV represented Ce^{3+} $3d_{5/2}$. Moreover, the bands labeled at 903.9 and 884.4 eV represent the $3d^{10}4f^1$ initial oxidation state corresponding to Ce^{3+}, while the peaks labeled at 916.15 and 898.0 eV represent the $3d^{10}4f^0$ final oxidation state corresponding to Ce^{4+}.[37] Ce 3d XPS spectrum shows a relatively small intensity Ce^{4+} emissions (916.15, 898.0 eV) compared to those for Ce^{3+} (903.9, 884.4 eV) indicating a reduced cerium oxide. The Ce^{4+}/Ce^{3+} valence ratio for the used catalyst was decreased from 2.82 to 1.97 resulting in an interconversion between Ce^{4+} and Ce^{3+} oxidation states indicating a reduction of some Ce^{4+} to Ce^{3+}.

The concentration of Ce^{3+} in ceria was determined by the following equation:[40]

$$\% \ Ce^{3+} = \frac{Peak \ area \ of \ Ce^{3+}}{Total \ peak \ area \ (Ce^{3+} + Ce^{4+})} \times 100 \tag{4}$$

For the fresh (as calcined) sample, the % Ce^{3+} was about 26% which increased to 34% for the used catalyst. However, a certain amount of Ce^{3+} was present, even in the fresh catalyst, which is probably due to the photo reduction of Ce^{4+} ions during the XPS experiments.[41] This change in the oxidation state of Ce (Ce^{4+} to Ce^{3+}) upon subsequent reduction leads to the formation of oxygen vacancies and releases free electrons, which in turn results in higher surface energy of the catalyst because of the increased adsorption capacity. This phenomenon is extremely important in CO methanation reaction, during which CO is adsorbed at an oxygen vacancy and subsequently reacts with hydrogen to produce methane. The addition of zirconium leads to improvements in ceria's oxygen storage capacity, redox property, thermal resistance, and an improved catalytic activity at low temperature.[42] Hori et al.[43] reported that the addition of ZrO_2 to form a Ce_x-$Zr_{1-x}O_2$ solid solution had the oxygen storage capacity values three to five times higher than that of pure CeO_2. In the CeO_2 cubic phase with ZrO_2 addition, the tetravalent cation Ce^{4+} has an eight-coordination of oxygen cations, and incorporation of zirconium into ceria lattice creates a high concentration of defects. Ce^{4+} (cationic radii = 1.09 Å) can be replaced by Zr^{4+} (0.86 Å) or by divalent Ni^{2+} (0.69 Å) and Co^{2+} (0.65 Å) cations to obtain more oxygen vacancies directly increasing the active sites for the reaction.[44,45]

The O1s spectra presented in Figure 3 (f) shows three different oxygen species located at 529.18, 529.71, and 531.13 eV. The peak located at 530.56−531.13 eV is due to the presence of lattice oxygen defect or the mobile oxygen. For the used catalyst, the O1s peaks tens to shift toward a higher B.E value as compared to the fresh catalyst under a decreased Ce^{4+}/Ce^{3+} valence ratio.[46,47] CO−TPD was conducted over the ZrO_2–CeO_2-based catalyst; the results are shown in Figure 5(a). The mechanism of desorption has been extensively studied over the past decade; however, it is a complex process and thus not always sufficiently understood. The rate of desorption is regarded as a function of the coverage (θ) according to the following equation[48]

$$r = Kf(\theta)e^{-E/RT} \tag{5}$$

where K is the rate constant, E is the desorption activation energy, and $f(\theta)$ is the fraction of the desorption site at θ. According to the above equation, the rate of desorption is a function of θ. Tanksale et al.[48] established that the rate of desorption is rapid at the low activation energy sites. For the ZrO_2–CeO_2 catalyst, a very sharp and high intensity peak was observed at a low temperature ($\leq$150 °C). This peak represents desorption at the low activation energy sites, which results in a low heat of adsorption and poor CO binding on the catalyst surface, with a corresponding high θ. This poor CO binding at a low temperature has low contribution toward methanation. The two chemisorption sites are believed to exist at low θ, whereas the single-site chemisorption prevails at higher θ. Figure 5 (a) shows single-site chemisorption at a high θ and low temperature range. A multisite chemisorption dominates between 150 and 350 °C at the cost of low θ, resulting in a high heat of adsorption, high CO adsorption capacity, and stronger contribution toward CH_4 formation. According to the literature,[48] the nature of the support plays an active role in
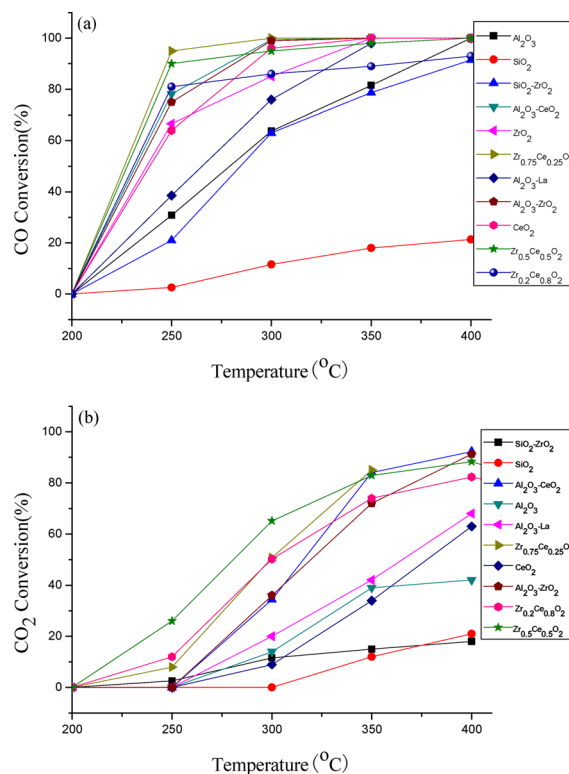
2252

dx.doi.org/10.1021/ie301399z | *Ind. Eng. Chem. Res.* 2013, 52, 2247−2256
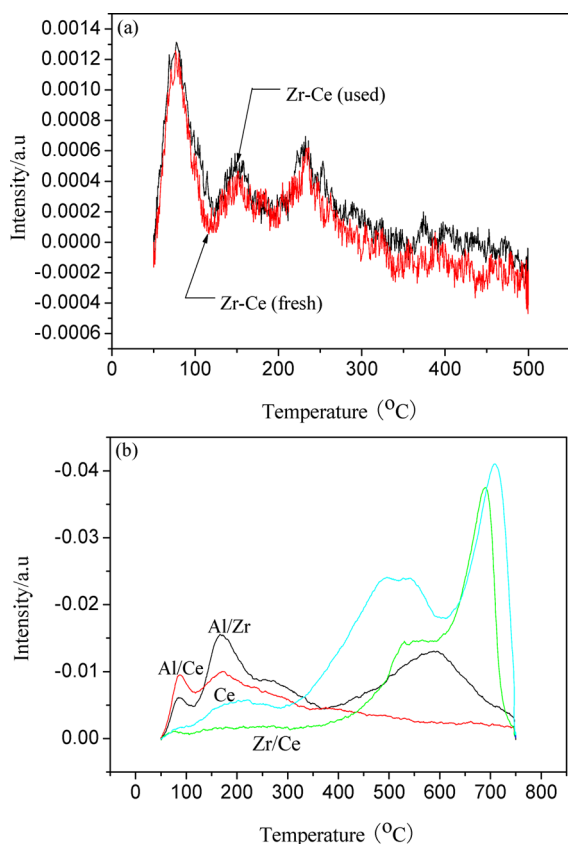
Figure 5. TPD profiles: (a) CO for ZrO_2-CeO_2 and (b) CO_2 for $Al_2O_3-ZrO_2$, $Al_2O_3-CeO_2$, Ce, and ZrO_2-CeO_2.

Figure 6. Effect of support composition on catalytic activity: (a) X_{CO} and (b) X_{CO2}.

determining the type of adsorption and the number of desorption sites because of the adsorption occurring on the different lattice spacing. The CO-TPD profile is similar for both the as-prepared and used catalysts, indicating high catalyst stability and CO adsorption capacity over a long period. The sample presents more than one TPD peak, indicating the presence of more than one active site for the adsorption of the reactant molecules.

The TPD profiles of the CO_2 adsorbed on the different catalysts are shown in Figure 5(b). The CO_2-TPD profiles of the $Al_2O_3-ZrO_2$- and $Al_2O_3-CeO_2$-supported catalysts show dominant low-temperature desorption peaks below 200 °C, which can be attributed to the weak basicity associated with the weakly adsorbed CO_2 on the catalyst surface. Meanwhile, the relatively high-temperature desorption peaks can be attributed to the strong basicity and consequently strong CO_2 adsorption. From the literature,[49] a low-temperature desorption peak may be attributed to the monodentate CO_2 adsorbed on the surface of the two catalysts. The peak with the high-temperature desorption may be assigned to the adsorbed bidentate CO_2. The CO_2 adsorbed on the weaker sites is desorbed at lower temperatures, whereas that adsorbed on the stronger sites is desorbed at higher temperatures. Consequently, the bidentate CO_2, which tends to bond to the oxide surface via two lattice oxygen ions, exhibits a higher desorption temperature compared to the monodentate CO_2. For the other two catalysts, CeO_2-only and ZrO_2-CeO_2, a very weak or no desorption peak was observed below 300 °C, indicating that both the basicity and the number of basic active sites were reduced. This phenomenon discouraged CO_2 binding onto the

surface of the catalyst to facilitate CO-catalyst interaction, resulting in the preferential CO hydrogenation to CH_4.

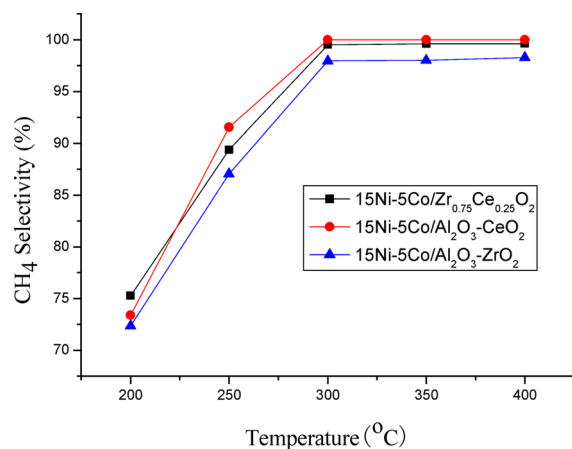Figure 6 shows catalytic properties of CO and CO_2 methanation on different support materials with 15 wt % Ni and 5 wt % Co. The SiO_2-supported catalyst with highest SSA showed the lowest activity, with a X_{CO} of only 20% at an elevated temperature of 400 °C. This indicates that the catalytic did not correlate with the SSA of the catalyst. The use of SiO_2-ZrO_2 significantly improved the catalytic activity, with 90% CO conversion at the same temperature. The use of the SiO_2-ZrO_2 support accelerated X_{CO}; however, a high reaction temperature was required, and only 15% CO_2 conversion at approximately 400 °C was achieved. Al_2O_3 support further enhanced X_{CO}, with 100% conversion attained at 400 °C. However, the X_{CO2} was only 30%. The XRD spectra show an improved active metal dispersion over the Al_2O_3-based catalysts with strong metal–support interaction. The use of a promoter (La_2O_3) enhanced the catalytic activity of Al_2O_3, with 98% X_{CO} at 350 °C and 60% X_{CO2} at 400 °C. The promoter not only enhanced the CO_2 conversion but also lowered the reaction temperature for CO methanation. Therefore, the use of CeO_2 was investigated to further promote CO_2 conversion. Previous studies[50,51] have revealed the promoting effect of cerium on the catalytic activity in CO_2 methanation through its oxidative–reductive property. XPS analysis reveals that oxygen vacancies were transferred from the bulk to the surface, which led to the formation of more active surface sites as well as to higher activity. The role of the mixed support loaded with 15 wt % Ni and 5 wt % Co was investigated to further enhance X_{CO} and X_{CO2} at a reduced reaction temperature. The catalysts with $Al_2O_3-ZrO_2$, $Al_2O_3-CeO_2$, and ZrO_2-CeO_2 supports showed complete X_{CO} at 295 °C, with approximately 90% X_{CO2} at 400

°C. Therdthianwong et al.[52] reported that the use of ZrO_2 significantly enhances the stability of the Ni/Al_2O_3 catalyst by promoting the dissociation of oxygen intermediates, enabling the reaction with the C-based species found on the surface of the active metal and limiting coke formation, which results in an extended catalyst life. The XRD results for the $Al_2O_3-ZrO_2$-supported catalyst show a uniform metal dispersion, which enhanced the metal−support interaction and resulted in lesser agglomeration, thereby leading to high catalytic activity. The catalyst with the ZrO_2-CeO_2 mixed-oxide support showed high-intensity diffraction peaks corresponding to ZrO_2 and metallic Ni, indicating a highly crystalline structure with a high degree of active metal reduction compared with other catalysts as indicated by XRD. The XPS analysis indicates that the reduced sample had a high concentration of active metal spcies on the surface of the carrier which resulted in a high methanation activity. Moreover, the Ni cations incorporated in the ZrO_2-CeO_2 structure, leading to an increase in its redox nature and enhancing the surface carbon hydrogenation to produce CH_4. Ocampo et al.[53] established that the decrease of the lattice parameter for the high Ni-loadings (10−15 wt %) suggests the incorporation of nickel ions into the ZrO_2-CeO_2 structure, as their ionic radius is smaller than zirconium ions radius (0.72 Å for Zr^{4+} versus 0.56 Å for Ni^{3+} or 0.69 Å for Ni^{2+}).

The formation of oxygen vacancy under a reduced Ce^{4+}/Ce^{3+} valence ratio results in an increased low temperature CO adsorption capacity also evident from CO-TPD results. The effect of support composition toward CO_x methanation activity in the CeO_2-ZrO_2-supported catalyst was also studied. Figure 6 shows that under varying CeO_2/ZrO_2 ratios, the $Zr_{0.75}Ce_{0.25}O_2$-supported sample exhibits the highest catalytic activity in comparison to $Zr_{0.5}Ce_{0.5}O_2$- and $Zr_{0.2}Ce_{0.8}O_2$-supported samples. The transformation from cerium rich cubic phase to zirconium rich tetragonal phase resulted in better activity of the $Zr_{0.75}Ce_{0.25}O_2$-supported catalyst. The selectivity for CH_4 at a given temperature did not significantly depend on the nature of the support but on the type of the active metal species. Figure 7 shows the results of methane selectivity over $Zr_{0.75}-Ce_{0.25}$, $Al_2O_3-CeO_2$, and $Al_2O_3-ZrO_2$ carriers. The results indicate that CH_4 selectivity increased with increasing temperature and reached (100%) at 300 °C over $Al_2O_3-CeO_2$ support followed by $Zr_{0.75}-Ce_{0.25}$ (S_{CH4} = 99%)

and $Al_2O_3-ZrO_2$ (S_{CH4} = 98%). At low reaction temperature (≤200 °C), CO_x methanation also results in the formation of some higher hydrocarbons (C_2-C_4) other than CH_4, but the formation was suppressed as the reaction temperature reached 300 °C with almost 100% methane selectivity.

3.3. Influence of GHSV. Figure 8 shows the influence of GHSV on the catalytic performance of the $15Ni-5Co/ZrO_2-$
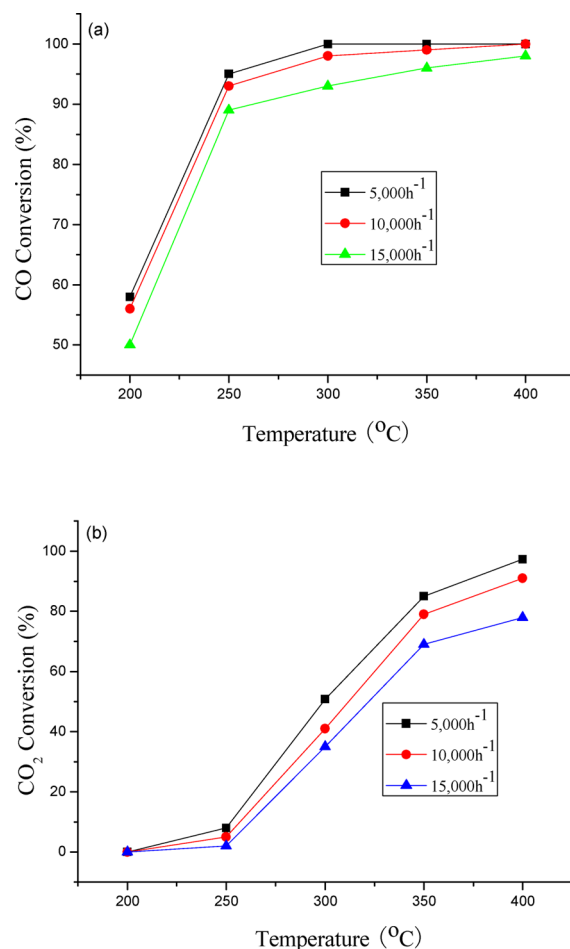
Figure 8. Effect of GHSV on CO_x methanation activity: (a) X_{CO} and (b) X_{CO2}.

CeO_2 catalyst for CO and CO_2 methanation reaction at the system pressure of 2.0 MPa. With the increase of GHSV, a decline in methanation activity of both CO and CO_2 was observed indicating that low GHSV is beneficial for methanation activity. However, for large scale industrial application CO_x methanation activity at a higher GHSV should be improved. Moreover, it was also revealed that a high (≥98%) CH_4 selectivity was maintained even at higher GHSV.

4. CONCLUSIONS

The ZrO_2-CeO_2-supported catalysts prepared via coprecipitation were found to be the most active and selective toward comethanation of CO and CO_2 in a gas mixture with a composition similar to that of a COG. Analysis of the catalytic structure as well as morphological studies indicate that the high catalytic activity of the ZrO_2-CeO_2-supported catalysts can be attributed to better metal−support interaction, higher active metal reduction, and an improved crystalline structure. Moreover, the ZrO_2-CeO_2 binary oxide support promotes

Figure 7. CH_4 selectivity over $Zr_{0.75}Ce_{0.25}$-, $Al_2O_3-CeO_2$-, and $Al_2O_3-ZrO_2$-supported catalysts.

the formation of oxygen vacancies under reduced Ce^{4+}/Ce^{3+} valence ratio, resulting in increased CO adsorption capacity and consequently higher catalytic activity. The Al_2O_3 support tends to have a stronger interaction with Ni and reacts to form $NiAl_2O_4$ spinels, resulting in a reduced catalytic activity. High GHSV has no significant effect on CO_x methanation and CH_4 selectivity.

■ **AUTHOR INFORMATION**

Corresponding Author

*(C.L.) Phone/Fax: +86-10-82544800. E-mail: csli@home.ipe. ac.cn. (S.Z.) Phone/Fax: +86-10-82627080. E-mail: sjzhang@ home.ipe.ac.cn.

Notes

The authors declare no competing financial interest.

■ **ACKNOWLEDGMENTS**

■ **REFERENCES**

(1) Yue, B.; Wang, X.; Ai, X.; Yang, J.; Li, L.; Lu, X.; Ding, W. Catalytic reforming of model tar compounds from hot coke oven gas with low steam/carbon ratio over Ni/MgO−Al₂O₃ catalysts. *Fuel Process. Technol.* **2010**, *91* (9), 1098−1104.

(2) Zhang, J.; Zhang, X.; Chen, Z.; Li, L. Thermodynamic and kinetic model of reforming coke-oven gas with steam. *Energy* **2010**, *35* (7), 3103−3108.

(3) Bermúdez, J. M.; Fidalgo, B.; Arenillas, A.; Menéndez, J. A. Dry reforming of coke oven gases over activated carbon to produce syngas for methanol synthesis. *Fuel* **2010**, *89* (10), 2897−2902.

(4) Zhang, Y.; Liu, J.; Ding, W.; Lu, X. Performance of an oxygen-permeable membrane reactor for partial oxidation of methane in coke oven gas to syngas. *Fuel* **2011**, *90* (1), 324−330.

(5) Cheng, H.; Yue, B.; Wang, X.; Lu, X.; Ding, W. Hydrogen production from simulated hot coke oven gas by catalytic reforming over Ni/Mg(Al)O catalysts. *J. Nat. Gas Chem.* **2009**, *18* (2), 225−231.

(6) Cheng, H.; Lu, X.; Hu, D.; Zhang, Y.; Ding, W.; Zhao, H. Hydrogen production by catalytic partial oxidation of coke oven gas in BaCo₀.₇Fe₀.₂Nb₀.₁O₃−δ membranes with surface modification. *Int. J. Hydrogen Energy* **2011**, *36* (1), 528−538.

(7) Yang, Z.; Ding, W.; Zhang, Y.; Lu, X.; Zhang, Y.; Shen, P. Catalytic partial oxidation of coke oven gas to syngas in an oxygen permeation membrane reactor combined with NiO/MgO catalyst. *Int. J. Hydrogen Energy* **2010**, *35* (12), 6239−6247.

(8) Panagiotopoulou, P.; Kondarides, D. I.; Verykios, X. E. Selective methanation of CO over supported noble metal catalysts: Effects of the nature of the metallic phase on catalytic performance. *Appl. Catal., A* **2008**, *344* (1−2), 45−54.

(9) Sabatier, P.; Senderens, J. B. New methane synthesis. *C. R. Acad. Sci. Paris* **1902**, *134*, 514−516.

(10) Kopyscinski, J.; Schildhauer, T. J.; Biollaz, S. M. A. Methanation in a fluidized bed reactor with high initial CO partial pressure: Part I—Experimental investigation of hydrodynamics, mass transfer effects, and carbon deposition. *Chem. Eng. Sci.* **2011**, *66* (5), 924−934.

(11) Fujita, S.-i.; Nakamura, M.; Doi, T.; Takezawa, N. Mechanisms of methanation of carbon dioxide and carbon monoxide over nickel/alumina catalysts. *Appl. Catal., A* **1993**, *104* (1), 87−100.

(12) Lee, G. D.; Moon, M. J.; Park, J. H.; Park, S. S.; Hong, S. S. Raney Ni catalysts derived from different alloy precursors Part II. CO and CO₂ methanation activity. *Korean J. Chem. Eng.* **2005**, *22* (4), 541−546.

(13) Hwang, K.-R.; Lee, C.-B.; Park, J.-S. Advanced nickel metal catalyst for water−gas shift reaction. *J. Power Sources* **2011**, *196* (3), 1349−1352.

(14) Koh, A. C. W.; Chen, L.; Kee Leong, W.; Johnson, B. F. G.; Khimyak, T.; Lin, J. Hydrogen or synthesis gas production via the partial oxidation of methane over supported nickel−cobalt catalysts. *Int. J. Hydrogen Energy* **2007**, *32* (6), 725−730.

(15) Czekaj, I.; Loviat, F.; Raimondi, F.; Wambach, J.; Biollaz, S.; Wokaun, A. Characterization of surface processes at the Ni-based catalyst during the methanation of biomass-derived synthesis gas: X-ray photoelectron spectroscopy (XPS). *Appl. Catal., A* **2007**, *329* (0), 68−78.

(16) Abe, T.; Tanizawa, M.; Watanabe, K.; Taguchi, A. CO2 methanation property of Ru nanoparticle-loaded TiO₂ prepared by a polygonal barrel-sputtering method. *Energy Environ. Sci.* **2009**, *2* (3), 315−321.

(17) Kustov, A. L.; Frey, A. M.; Larsen, K. E.; Johannessen, T.; Nørskov, J. K.; Christensen, C. H. CO methanation over supported bimetallic Ni−Fe catalysts: From computational studies towards catalyst optimization. *Appl. Catal., A* **2007**, *320* (0), 98−104.

(18) Aksoylu, A. E.; Mısırlı, Z.; Önsan, Z. İ. Interaction between nickel and molybdenum in Ni−Mo/Al₂O₃ catalysts: I: CO₂ methanation and SEM-TEM studies. *Appl. Catal., A* **1998**, *168* (2), 385−397.

(19) Ocampo, F.; Louis, B.; Kiwi-Minsker, L.; Roger, A.-C. Effect of Ce/Zr composition and noble metal promotion on nickel based CeₓZr₁₋ₓO₂ catalysts for carbon dioxide methanation. *Appl. Catal., A* **2011**, *392* (1−2), 36−44.

(20) Sharma, S.; Hu, Z.; Zhang, P.; McFarland, E. W.; Metiu, H. CO₂ methanation on Ru-doped ceria. *J. Catal.* **2011**, *278* (2), 297−309.

(21) Wang, Y.; Wu, R.; Zhao, Y. Effect of ZrO₂ promoter on structure and catalytic activity of the Ni/SiO2 catalyst for CO methanation in hydrogen-rich gases. *Catal. Today* **2010**, *158* (3−4), 470−474.

(22) Kok, E.; Cant, N.; Trimm, D.; Scott, J. The effect of support and synthesis method on the methanation activity of alumina-supported cobalt−ruthenium−lanthana catalysts. *Catal. Today* **2011**, *178* (1), 79−84.

(23) Jiménez, V.; Sánchez, P.; Panagiotopoulou, P.; Valverde, J. L.; Romero, A. Methanation of CO, CO₂ and selective methanation of CO, in mixtures of CO and CO2, over ruthenium carbon nanofibers catalysts. *Appl. Catal., A* **2010**, *390* (1−2), 35−44.

(24) Sehested, J.; Dahl, S.; Jacobsen, J.; Rostrup-Nielsen, J. R. Methanation of CO over nickel: mechanism and kinetics at high H₂/CO ratios. *J. Phys. Chem. B* **2004**, *109* (6), 2432−2438.

(25) Zyryanova, M. M.; Snytnikov, P. V.; Amosov, Y. I.; Kuzmin, V. A.; Kirillov, V. A.; Sobyanin, V. A. Design, scale-out, and operation of a preferential CO methanation reactor with a nickel−ceria catalyst. *Chem. Eng. J.* **2011**, *176−177* (0), 106−113.

(26) Fujita, S.-I.; Takezawa, N. Difference in the selectivity of CO and CO₂ methanation reactions. *Chem. Eng. J.* **1997**, *68* (1), 63−68.

(27) Habazaki, H.; Yamasaki, M.; Zhang, B.-P.; Kawashima, A.; Kohno, S.; Takai, T.; Hashimoto, K. Co-methanation of carbon monoxide and carbon dioxide on supported nickel and cobalt catalysts prepared from amorphous alloys. *Appl. Catal., A* **1998**, *172* (1), 131−140.

(28) Wang, W.; Wang, S.; Ma, X.; Gong, J. Recent advances in catalytic hydrogenation of carbon dioxide. *Chem. Soc. Rev.* **2011**, *40* (7), 3703−3727.

(29) Eckle, S.; Anfang, H.-G.; Behm, R. J. What drives the selectivity for CO methanation in the methanation of CO₂-rich reformate gases on supported Ru catalysts. *Appl. Catal., A* **2011**, *391* (1−2), 325−333.

(30) Jacquemin, M.; Beuls, A.; Ruiz, P. Catalytic production of methane from CO₂ and H₂ at low temperature: Insight on the reaction mechanism. *Catal. Today* **2010**, *157* (1−4), 462−466.

(31) Panagiotopoulou, P.; Kondarides, D. I.; Verykios, X. E. Selective methanation of CO over supported Ru catalysts. *Appl. Catal., B* **2009**, *88* (3−4), 470−478.

2255

dx.doi.org/10.1021/ie301399z | *Ind. Eng. Chem. Res.* 2013, 52, 2247−2256

(32) Grosvenor, A. P.; Biesinger, M. C.; Smart, R. S. C.; McIntyre, N. S. New interpretations of XPS spectra of nickel metal and oxides. *Surf. Sci.* **2006**, *600* (9), 1771−1779.

(33) Lin, S. S. Y.; Kim, D. H.; Engelhard, M. H.; Ha, S. Y. Water-induced formation of cobalt oxides over supported cobalt/ceria–zirconia catalysts under ethanol-steam conditions. *J. Catal.* **2010**, *273* (2), 229−235.

(34) Pérez-Hernández, R.; Gutiérrez-Martínez, A.; Palacios, J.; Vega-Hernández, M.; Rodríguez-Lugo, V. Hydrogen production by oxidative steam reforming of methanol over Ni/CeO$_2$−ZrO$_2$ catalysts. *Int. J. Hydrogen Energy* **2011**, *36* (11), 6601−6608.

(35) Srisiriwat, N.; Therdthianwong, S.; Therdthianwong, A. Oxidative steam reforming of ethanol over Ni/Al2O3 catalysts promoted by CeO$_2$, ZrO$_2$ and CeO$_2$−ZrO$_2$. *Int. J. Hydrogen Energy* **2009**, *34* (5), 2224−2234.

(36) Oh, Y.-S.; Roh, H.-S.; Jun, K.-W.; Baek, Y.-S. A highly active catalyst, Ni/Ce−ZrO$_2$/γ-Al$_2$O$_3$, for on-site H2 generation by steam methane reforming: pretreatment effect. *Int. J. Hydrogen Energy* **2003**, *28* (12), 1387−1392.

(37) Nelson, A. E.; Schulz, K. H. Surface chemistry and micro-structural analysis of Ce$_x$Zr$_{1−x}$O$_2$−y model catalyst surfaces. *Appl. Surf. Sci.* **2003**, *210* (3−4), 206−221.

(38) Bêche, E.; Charvin, P.; Perarnau, D.; Abanades, S.; Flamant, G. Ce 3d XPS investigation of cerium oxides and mixed cerium oxide (Ce$_x$Ti$_y$O$_z$). *Surf. Interface Anal.* **2008**, *40* (3−4), 264−267.

(39) Wang, Z.; Qu, Z.; Quan, X.; Wang, H. Selective catalytic oxidation of ammonia to nitrogen over ceria−zirconia mixed oxides. *Appl. Catal., A* **2012**, *411−412* (0), 131−138.

(40) Zhang, F.; Wang, P.; Koberstein, J.; Khalid, S.; Chan, S.-W. Cerium oxidation state in ceria nanoparticles studied with X-ray photoelectron spectroscopy and absorption near edge spectroscopy. *Surf. Sci.* **2004**, *563* (1−3), 74−82.

(41) Serrano-Ruiz, J. C.; Huber, G. W.; Sánchez-Castillo, M. A.; Dumesic, J. A.; Rodríguez-Reinoso, F.; Sepúlveda-Escribano, A. Effect of Sn addition to Pt/CeO$_2$−Al$_2$O$_3$ and Pt/Al$_2$O$_3$ catalysts: An XPS, 119Sn Mössbauer and microcalorimetry study. *J. Catal.* **2006**, *241* (2), 378−388.

(42) Thammachart, M.; Meeyoo, V.; Risksomboon, T.; Osuwan, S. Catalytic activity of CeO2−ZrO2 mixed oxide catalysts prepared via sol−gel technique: CO oxidation. *Catal. Today* **2001**, *68* (1−3), 53−61.

(43) Hori, C. E.; Permana, H.; Ng, K. Y. S.; Brenner, A.; More, K.; Rahmoeller, K. M.; Belton, D. Thermal stability of oxygen storage properties in a mixed CeO2-ZrO2 system. *Appl. Catal., B* **1998**, *16* (2), 105−117.

(44) Lin, X.-M.; Li, L.-P.; Li, G.-S.; Su, W.-H. Transport property and Raman spectra of nanocrystalline solid solutions Ce$_{0.8}$Nd$_{0.2}$O$_2$−δ with different particle size. *Mater. Chem. Phys.* **2001**, *69* (1−3), 236−240.

(45) Pengpanich, S.; Meeyoo, V.; Rirksomboon, T.; Bunyakiat, K. Catalytic oxidation of methane over CeO$_2$-ZrO$_2$ mixed oxide solid solution catalysts prepared via urea hydrolysis. *Appl. Catal., A* **2002**, *234* (1−2), 221−233.

(46) Wang, H.; Chen, Y.; Zhang, Q.; Zhu, Q.; Gong, M.; Zhao, M. Catalytic methanol decomposition to carbon monoxide and hydrogen over Pd/CeO$_2$-ZrO$_2$-La$_2$O$_3$ with different Ce/Zr molar ratios. *J. Nat. Gas Chem.* **2009**, *18* (2), 211−216.

(47) Kim, S. H.; Nam, S.-W.; Lim, T.-H.; Lee, H.-I. Effect of pretreatment on the activity of Ni catalyst for CO removal reaction by water−gas shift and methanation. *Appl. Catal., B* **2008**, *81* (1−2), 97−104.

(48) Tanksale, A.; Beltramini, J. N.; Dumesic, J. A.; Lu, G. Q. Effect of Pt and Pd promoter on Ni supported catalysts—A TPR/TPO/TPD and microcalorimetry study. *J. Catal.* **2008**, *258* (2), 366−377.

(49) Li, L.; Song, L.; Wang, H.; Chen, C.; She, Y.; Zhan, Y.; Lin, X.; Zheng, Q. Water-gas shift reaction over CuO/CeO$_2$ catalysts: Effect of CeO$_2$ supports previously prepared by precipitation with different precipitants. *Int. J. Hydrogen Energy* **2011**, *36* (15), 8839−8849.

(50) Rynkowski, J. M.; Paryjczak, T.; Lewicki, A.; Szynkowska, M. I.; Maniecki, T. P.; Jozwiak, W. K. Characterization of Ru/CeO$_2$-Al$_2$O$_3$ catalysts and their performance in CO$_2$ methanation. *React. Kinet. Catal. Lett.* **2000**, *71* (1), 55−64.

(51) Trovarelli, A.; Deleitenburg, C.; Dolcetti, G.; Lorca, J. L. CO$_2$ methanation under transient and steady-state conditions over Rh/CeO$_2$ and CeO$_2$-promoted Rh/SiO$_2$: The role of surface and bulk ceria. *J. Catal.* **1995**, *151* (1), 111−124.

(52) Therdthianwong, S.; Therdthianwong, A.; Siangchin, C.; Yongprapat, S. Synthesis gas production from dry reforming of methane over Ni/Al$_2$O$_3$ stabilized by ZrO$_2$. *Int. J. Hydrogen Energy* **2008**, *33* (3), 991−999.

(53) Ocampo, F.; Louis, B.; Roger, A.-C. Methanation of carbon dioxide over nickel-based Ce$_{0.72}$Zr$_{0.28}$O2 mixed oxide catalysts prepared by sol−gel method. *Appl. Catal., A* **2009**, *369* (1−2), 90−96.

2256

dx.doi.org/10.1021/ie301399z | *Ind. Eng. Chem. Res.* 2013, 52, 2247−2256